DOI: 10.1103/PhysRevMaterials.6.064402
Report number: FERMILAB-PUB-22-544-SQMS
(accepted)

Stability, Metallicity, and Magnetism in Niobium Silicide Nanofilms

Xuezeng Lu,[1] Dominic P. Goronzy,[1,2] Carlos G. Torres-Castanedo,[1] Paul Masih Das,[1] Maryam Kazemzadeh-Atoufi,[1] Anthony McFadden,[3] Corey Rae H. McRae,[4,5] Peter W. Voorhees,[1] Vinayak P. Dravid,[1,6] Michael J. Bedzyk,[1,7,8] Mark C. Hersam,[1,9,10] and James M. Rondinelli[1,*]

[1] *Department of Materials Science and Engineering, Northwestern University, Evanston, Illinois 60208, United States*

[2] *International Institute for Nanotechnology, Northwestern University, Evanston, Illinois 60208, United States*

[3] *National Institute of Standards and Technology, Boulder, Colorado 80305, United States*

[4] *Department of Electrical, Computer & Energy Engineering, University of Colorado Boulder, Boulder, Colorado 80309, United States*

[5] *Department of Physics, University of Colorado, Boulder, Colorado 80309, United States*

[6] *Northwestern University Atomic and Nanoscale Characterization Experimental Center (NUANCE), Northwestern University, Evanston, Illinois 60208, United States*

[7] *Department of Physics and Astronomy, Northwestern University, Evanston, Illinois 60208, United States*

[8] *Applied Physics Program, Northwestern University, Evanston, Illinois 60208, United States*

[9] *Department of Chemistry, Northwestern University, Evanston, Illinois 60208, United States*

[10] *Department of Electrical and Computer Engineering, Northwestern University, Evanston, Illinois 60208, United States*

*Email: jrondinelli@northwestern.edu

KEYWORDS: superconducting qubits, density functional calculations, transmission electron microscopy, X-ray reflectivity, niobium silicide nanofilm, phase stability

Abstract

Modern superconducting qubits based on two-dimensional (2D) transmons typically involve the growth of Nb thin films on high-resistivity Si substrates. Since imperfections at the Nb-Si hetero-interface have been implicated as a source of two-level systems that limit quantum coherence times, detailed characterization and understanding of niobium silicide interfacial layers are critical to improving superconducting qubit technology. While bulk binary intermetallic niobium silicide phases are well understood, the thermodynamic phase stability and properties of ultrathin niobium silicides, such as those that found at the Nb-Si heterointerface in 2D transmons, have not yet been explored. Here, we report finite-size effects for ultrathin niobium silicide films using density functional theory calculations and predict nanoscale stabilization of Nb_6Si_5 over the bulk α-Nb_5Si_3 phase. This result is consistent with our experimental observations of a niobium silicide interfacial layer between a sputtered Nb thin film and the underlying Si substrate. Furthermore, our calculations show that Nb_6Si_5 nanofilms are nonmagnetic, making them superior to nanofilms of α-Nb_5Si_3 that exhibit antiferromagnetic correlations detrimental to long coherence times in superconducting qubits. By providing atomic-scale insight into niobium silicide nanofilms, this work can help guide ongoing efforts to optimize Nb-Si heterointerfaces for long coherence times in superconducting qubits.

INTRODUCTION

Two-dimensional (2D) transmons, which are widely used in superconducting qubit technology, often involve the growth of niobium thin films on high-resistivity silicon substrates [1–3]. Previous reports pertaining to device performance of transmons have shown that interfacial composition and structure can affect the coherence time of superconducting qubits [4–7]. Since niobium and silicon are known to form bulk binary intermetallic niobium silicides that exhibit a range of stable compositions [5,8–12], it is likely that niobium silicide interfacial layers are present in 2D transmon architectures. Previous bulk niobium silicide structural studies have focused on understanding the phase stability and microstructure evolution from room temperature to 2600℃, [5,6,9–18] where the relevant high-temperature silicides are Nb_3Si and β-Nb_5Si_3 [18] and the low-temperature silicides are α-Nb_5Si_3, NbSi, and $NbSi_2$. In addition, the superconducting properties of three polymorphs of Nb_3Si and NbSi have been explored [17]. On the other hand, the thermodynamic phase stability of niobium silicides in the ultrathin regime, which are likely to be present at the Nb-Si heterointerface, has not yet been reported, despite their likely role in influencing coherence times of superconducting qubits [3,19,20]. Although previous X-ray diffraction and reflectivity studies suggested that the interfacial Nb-Si composition changes from Nb_3Si to $NbSi_2$ through coexistence of Nb_3Si and Nb_5Si_3 with increasing temperature [13,14], this model is inconsistent with the nanometer-scale niobium silicides observed at the Nb-Si heterointerface in 2D transmons. Consequently, a thorough atomic-scale investigation of niobium silicide nanofilms is desirable to understand and mitigate potential sources of two-level systems (TLSs) that compromise coherence times in superconducting qubits.

Here, we investigate finite-size effects on the stability and properties of niobium silicide nanofilms using a combination of first-principles calculations, X-ray reflectivity (XRR), and transmission electron microscopy (TEM). Our density functional theory (DFT) calculations show that a transition in the stable silicide from α-Nb_5Si_3 to Nb_6Si_5 occurs as the film thickness decreases due to vibrational entropy contributions, along with a decrease in carrier density for both phases. These thickness-dependent predictions of the silicide composition are consistent with XRR and TEM measurements on niobium silicides found in interfacial layers between a sputtered Nb thin film and the underlying silicon substrate. Furthermore, our calculations indicate that niobium silicide nanofilms are nonmagnetic in contrast to bulk α-Nb_5Si_3, which exhibits itinerant antiferromagnetism at its surface that provides dissipation channels beyond localized paramagnetic defects. Overall, this study provides atomic-scale insight into ultrathin niobium silicides that is likely to inform processing methods aimed at maximizing coherence time in superconducting qubits.

METHODS

First-principles calculations

Our total energy calculations were based on density functional theory (DFT) within the generalized gradient approximation (GGA) utilizing the SCAN functional [21,22] implemented in the Vienna *Ab Initio* Simulation Package (VASP) [23,24]. We used a 400 eV plane wave cutoff energy for all calculations and the projector augmented wave (PAW) method [25,26] with Nb 5*s*, 4*p*, and 4*d* electrons, and Si 3*s* and 3*p* electrons treated as valence states, except for the phonon calculations where we used a 500 eV cutoff energy. We testified that the slab calculations with energy cutoff of 500eV lead to total energy differences less than 1 meV/atom compared to those with an energy cutoff of 400eV. The *k*-point meshes for Nb_3Si, Nb_2Si, α-Nb_5Si_3, β-Nb_5Si_3, γ-Nb_5Si_3, Nb_3Si_2, Nb_5Si_4, Nb_6Si_5, NbSi and $NbSi_2$ are set to 3×3×6, 6×6×6, 6×6×3, 3×3×6, 4×4×6, 4×4×6, 4×4×2, 5×3×2, 10×10×6, 8×8×6, respectively, for their conventional unit cell. The *k*-point meshes for nanofilms of Nb_3Si, α-Nb_5Si_3, β-Nb_5Si_3, γ-Nb_5Si_3, Nb_3Si_2, Nb_5Si_4, Nb_6Si_5, NbSi and $NbSi_2$ are set to 4×4×1, 6×6×1, 4×4×1, 6×6×1, 6×6×1, 4×4×1, 5×2×1, 7×6×1, 6×6×1, respectively, as indicated in Table 1. In the slab calculations, the number of *k* points along each direction satisfies $k_i \cdot a_i >$ 40, where k_i and a_i are the number of *k* points and lattice parameters along direction *i=x, y, z*, respectively. Then the total energy differences are less than 1 meV/atom upon further increasing the density of the *k*-point meshes. Gaussian smearing (0.10 eV width) for the Brillouin-zone integrations is used for the metals. In the surface calculations, both the internal atomic positions and the in-plane lattice parameters are fully relaxed along with the out-of-plane lattice parameter, which includes the addition of 15 Å of vacuum.

When investigating the magnetic spin orders in the nanofilm of α-Nb_5Si_3, the DFT plus Hubbard *U* method [27] is used with the Hubbard *U* and the exchange parameter *J* set to 3 eV and 1 eV, respectively. The same *U* and *J* values are also applied to bulk α-Nb_5Si_3 and *bcc* Nb for computing the formation energy with the magnetic orders in the surface, where the magnetic moment on the Nb is set to zero.

Formation energy calculations

The formation energy ($E_{x/y}$) of these Nb$_x$Si$_y$ bulk phases and surface structures are calculated by the following formula:

$$E_{x/y} = (E_{\mathrm{Nb}_x\mathrm{Si}_y} - xE_{\mathrm{Nb}} - yE_{\mathrm{Si}})/(x+y) \quad (1)$$

where $E_{\mathrm{Nb}_x\mathrm{Si}_y}$ is the total energy of various Nb$_x$Si$_y$ at the ground state; E_{Nb} and E_{Si} are the mono-atomic energy of the Nb atom and Si atom in their bulk phases, respectively.

By considering the temperature effects on the formation energy, we added the temperature-dependent part of the electronic free energy (E_{el}) and the phononic free energy (E_{ph}) as in ref [28]. The electronic free energy is written as:

$$E_{el}(V,T) = H_{el}(V,T) - TS_{el}(V,T) \quad (2)$$

where the electronic DOS (g_e) and Fermi-Dirac distribution function (*f*) are used to compute the electronic enthalpy and entropy, which can be expressed as:

$$H_{el}(V,T) = \int_{-\infty}^{+\infty} g_e(\varepsilon)\cdot f(\varepsilon)\cdot \varepsilon d\varepsilon - \int_{-\infty}^{\varepsilon_F} g_e(\varepsilon)\cdot \varepsilon d\varepsilon \quad (3)$$

and

$$S_{el}(V,T) = -k_B \int_{-\infty}^{+\infty} g_e(\varepsilon)\cdot \{f(\varepsilon)\ln[f(\varepsilon)] + [1-f(\varepsilon)]\ln[1-f(\varepsilon)]\}d\varepsilon \quad (4)$$

The phononic free energy is written as:

$$E_{ph}(V,T) = \frac{1}{N_q}\sum_{q,\sigma}\frac{\hbar\omega_{q,\sigma}}{2} + k_BT\cdot\log\left[1-\exp\left(-\frac{\hbar\omega_{q,\sigma}}{k_BT}\right)\right] \quad (5)$$

where q and σ represent the reciprocal coordinate and phonon branch, respectively; ω is the vibrational frequency.

Here, the harmonic phonons and electronic DOS at the equilibrium volume *V* are used to efficiently calculate the free energies, which are especially suitable for a moderate temperature range less than 1000 K since the effects of thermal expansion in the free energies are usually small [29,30], and expected to be even less important in some relative free energies (*e.g.*, formation free energy considered here).

The formation free energy at finite temperature includes the electronic free energy and phononic free energy as:

$$E_{x/y}^{T} = E_{x/y}^{DFT} + [E_{el}^{\mathrm{Nb}_x\mathrm{Si}_y} + E_{ph}^{\mathrm{Nb}_x\mathrm{Si}_y} - x(E_{el}^{\mathrm{Nb}} + E_{ph}^{\mathrm{Nb}}) - y(E_{el}^{\mathrm{Si}} + E_{ph}^{\mathrm{Si}})]/(x + y). \qquad (6)$$

Niobium thin film preparation

Si (111) wafers, 76.2 mm diameter, (WaferPro, Santa Clara, CA) were prepared with the standardized RCA cleaning procedure and then hydrogen passivated using a wet chemical treatment established for Si(111). [31] Following passivation, wafers were immediately placed in a transport vessel and sealed in an Ar environment. Wafers were shipped to the Quantum Processing Group at NIST for Nb deposition within 24 hrs of hydrogen passivation. During transfer from the shipping container to the load lock, the sample was briefly exposed to atmosphere. The sample was loaded into a sputtering tool having a base pressure below 1×10^{-8} Torr equipped with reflection high-energy electron diffraction (RHEED) for surface analysis. RHEED patterns taken of the H:Si(111) indicated a crystalline, unreconstructed surface. A 40 nm thick Nb film was deposited using DC magnetron sputtering at a pressure of 3 mTorr with 15 sccm Ar flow from a 3-inch diameter Nb target having a metals basis purity of 99.95%. A 300 W sputtering power was used, resulting in a deposition rate of 1.3A/sec which was monitored using a quartz crystal microbalance. The film was deposited at room temperature. After Nb deposition, RHEED patterns were observed to be consistent with a textured Nb(110) surface.

Transmission electron microscopy

Cross-sectional TEM samples of Nb thin films were performed using conventional focused ion beam (FIB) liftout on a Ga^+-based Helios Nanolab operating at 30 kV. A spherical aberration corrected JEOL ARM200CF microscope operating at 200 kV was utilized to acquire high-resolution scanning TEM (STEM) images perpendicular to the Nb [110] zone axis. Images were collected with a JEOL annular dark field (90-370 mrad) detector under an 8 µs dwell time and low pass filtered using ImageJ. Stoichiometric STEM-EDS was conducted with dual Oxford silicon drift detectors.

X-ray reflectivity

XRR measurements were performed with a Smartlab SE diffractometer equipped with a 9 kW Cu rotating anode operated at 45 kV and 160 mA. A Ge (220) 2-bounce monochromator was utilized to have a monochromatic beam (λ = 1.5406 Å). The collimated beam was 0.1 x 5 mm^2. XRR measurements are plotted in terms of the scattering vector $Q = 4\pi \sin(\theta)/\lambda$, normalized to the measured incident beam intensity, and corrected for geometrical footprint and background signal. The XRR analysis was performed using Motofit software [32]. The XRR fitting is obtained from electron density profiles that simulate the Si/Nb_xSi_y/Nb/NbO/Nb_2O_5 heterostructure. The stochiometric determination of Nb_xSi_y was obtained from fitting the electron density of this layer.

RESULTS AND DISCUSSION

Bulk niobium silicide phase stability

At room temperature, the most stable structure for bulk niobium silicide is α-Nb_5Si_3, exhibiting tetragonal *I*4/*mcm* symmetry, where it adopts the Cr_5B_3 prototype structure with four formula units in a conventional cell [9,11,18]. The Nb cations form Nb_{10} and Nb_{12} polyhedra, which coordinate anionic Si monomers and Si-Si dimers of length $d = 2.4$ Å (**Figure 1**). α-Nb_5Si_3 may be described as a valence-precise compound as $(\mathrm{Nb}^{3+})_5(\mathrm{Si}^{4-})(\mathrm{Si}_2^{6-})(5e^-)$ using Zintl bonding principles [21,22], which implies that Nb has a nominal $4d^2$ electronic configuration (the +2-oxidation state for Nb is eliminated because this would make α-Nb_5Si_3 a diamagnetic semiconductor, whereas it exhibits metallic conductivity [11,35]). Although Nb 4*d* – Si 3*p* orbital hybridization restricts full electron transfer, both anions are diamagnetic with closed-shell configurations. Thus, we expect the remaining five delocalized electrons to occupy the Nb 4d orbitals participating in Nb-Nb and Nb-Si bonding. Overall, these features make bulk α-Nb_5Si_3 a metallic paramagnet.

Our calculated electronic density-of-states (DOS) shows that the Fermi level is indeed located in a region with a large number of states consisting of multiple fractionally occupied Nb 4*d* orbitals (**Figure 2a**). There are approximately 0.41 states per Nb-*d* orbital, leading to an itinerant electron gas in the open 4*d* shell of Nb. We find Si 3*s* states with σ_g bonding and σ_u^* antibonding characters located between -12 eV and -8 eV, as confirmed from our projected crystal orbital Hamilton population (COHP) analysis [36–38] (**Figure 2a**), indicating the presence of the Zintl Si_2^{6-} dimers. Modest hybridization exists between the Nb and Si orbitals throughout the entire energy range, with the Nb 4*d* states spanning -6 eV to 3 eV. Metallic Nb-Nb bonding mainly occurs over the energy range from -3 eV to 2.5 eV and leads to the formation of the pseudogap in the DOS, which separates the filled bonding states from the empty antibonding states. The Fermi energy is located in a region just above the pseudogap, which can lead to compositional disorder or the formation of a glass state in intermetallic phases [39]. The electron filling for stoichiometric α-Nb_5Si_3 is such that the Fermi level is just above this minimum energy, suggesting that reducing the number of valence electrons could shift the Fermi level to lower energy through defect formation or deviations from pristine stoichiometry.

With increasing temperature, niobium silicides with different compositions form. We computed the Nb-Si convex hull by selecting low-energy niobium silicide compositions with their prototype structures specified in parentheses based on previous studies [9,11]: Nb_3Si (PTi_3), Nb_2Si (Au_2Cu), α-Nb_5Si_3 (Cr_5B_3), β-Nb_5Si_3 (W_5Si_3), γ-Nb_5Si_3 (Mn_5Si_3), Nb_3Si_2 (U_3Si_2), Nb_5Si_4 (Zr_5Si_4), Nb_6Si_5 (Ti_6Ge_5), NbSi (FeB), and $NbSi_2$ ($CrSi_2$). The Nb_2Si (Si_2^{4-}), Nb_5Si_3-β (Si_2^{4-} and Si^{4-}), Nb_5Si_3-γ (Si_2^{4-}), Nb_3Si_2 (Si_2^{6-}), Nb_5Si_4 (Si_2^{6-}), Nb_6Si_5 (Si_4^{4-}, Si_2^{4-} and $\mathrm{Si'}_2^{4-}$) and NbSi (Si_2^{4-}) compositions can also be regarded as the Zintl phases [34], where the Zintl anions are specified in parentheses (**Figure 1**). One calculation [9] found that Nb_2Si is closer to the hull than NbSi, whereas another calculation [11] reported that NbSi is closer to the hull than Nb_2Si. Our 0 K convex hull obtained from DFT using the strongly constrained and appropriately normed (SCAN) functional reproduces the previously reported convex hull and reconciles this controversy. Our results show that both phases are close to the hull. In addition, our calculations using the SCAN functional further confirmed that the $NbSi_2$ has $P6_222$ symmetry, in contrast to the previously reported *Fddd* structure [12]. These findings indicate that DFT-SCAN is a suitable level of theory to describe niobium silicides and thus was chosen to compute thickness effects in niobium silicide nanofilms.

Figure 2b shows that the convex hull is determined by α-Nb_5Si_3 and $NbSi_2$, which is consistent with the experimental phase diagram [18] since they are the low-temperature stable silicides. Nb_3Si is also very close to the convex hull (~11.4 meV/atom from the hull) because it is experimentally stable over the 1765 – 1915°C range [18]. For the other compositions above the hull, we find that β-Nb_5Si_3 and Nb_3Si_2 have formation energies of ~37 meV/atom higher than α-Nb_5Si_3. We then calculated the thermal stability of the low-temperature phases (*i.e.*, α-Nb_5Si_3 and $NbSi_2$) by including the temperature-dependent part of the electronic free energy and the vibrational free energy (see **Methods** and **Figure S1** [40]). We excluded β-Nb_5Si_3-β [9,18] from this calculation and instead focused on Nb_3Si_2 and Nb_6Si_5, because as we show below, Nb_6Si_5 is stabilized by finite-size effects. Here, we find that Nb_3Si_2 becomes stable at intermediate temperatures, ranging from ~500 K to 1500 K between the previously reported α-Nb_5Si_3 and $NbSi_2$ phases forming the convex hull at 0 K.

Niobium silicide nanofilm phase stability

Next, we investigate the phase stability for the niobium silicides in unsupported nanofilm geometries including surface and finite thickness effects. We allow for relaxation normal to the film, no surface reconstruction, and no adsorption. Favorable surface orientations and compositions for the different silicide phases are created by conducting an atomic population analysis (*i.e.*, density-derived electrostatic and chemical (DDEC) analysis [41,42]). The overlap population is expressed as:

$$A_{i,j}|_{i\neq j} = 2\int \frac{\rho_i(\boldsymbol{r_i})\rho_j(\boldsymbol{r_j})}{\rho(\boldsymbol{r})} d^3\boldsymbol{r} \qquad (1)$$

where $A_{i,j}$ is the overlap population (OP), and $\boldsymbol{r_i}$ and r_j are the positions for atoms *i* and *j*, respectively. Using Equation 1, we define the [*h k l*] directional-dependent OP as:

$$OP_{hkl} = \sum_i^N \frac{1}{2} A_{i,j}|_{i\neq j} \left| \frac{(\boldsymbol{r_j}-\boldsymbol{r_i})\cdot\boldsymbol{R}}{|\boldsymbol{r_j}-\boldsymbol{r_i}||\boldsymbol{R}|} \right| \qquad (2)$$

where we consider the summation of the OP among the nearest-neighboring atoms j for all the atoms i in the unit cell along a specified direction $\boldsymbol{R}$ with Miller indices h, k, and l. If OP_{hkl} is small along a direction, we consider that the energetic cost to break the bonds along this direction is also small. Small OP_{hkl}, therefore, would correspond to plane normal directions for likely cleavage planes to generate finite-sized two-dimensional silicide nanofilms.

With this method, we find that the OP_{hkl} value is the smallest along the [001] direction in α-Nb_5Si_3, which is consistent with a previous detailed first-principles study on the surface of α-Nb_5Si_3 [8,33]. The surface directions for the other compositions are [001] for Nb_3Si, [111] for Nb_2Si, [001] for β-Nb_5Si_3, [001] for γ-Nb_5Si_3, [001] for Nb_3Si_2, [001] for Nb_5Si_4, [100] for Nb_6Si_5, [100] for NbSi, and [001] for $NbSi_2$ (**Tables S2-S11** [40]). We then determined the two surface terminations for each slab structure along these directions using a layer-resolved OP_{hkl}, where the surface termination is selected base on the layer giving the smallest OP_{hkl} value (**Tables S12-S17** [40]). Throughout, we use symmetric slab geometries with identical surface terminations (**Figure 3**).

Using these slab structures, we then compute the surface energies according to the expression [8]:

$$\gamma = \frac{1}{2A}\left[E_{\mathrm{slab}} - \frac{1}{n_s} N_{\mathrm{Si}} \mu^{\mathrm{bulk}}_{\mathrm{Nb}_{n_n} Si_{n_s}} - \left(N_{\mathrm{Nb}} - \frac{n_n}{n_s} N_{\mathrm{Si}}\right) \mu_{\mathrm{Nb}}\right] \qquad (3)$$

where γ is the surface energy, E_{slab} is the 0 K total energy of the slab structure, A is the surface area, n_n and n_s are the number of Nb and Si atoms in the specified niobium silicide phases, respectively. N_{Nb} and N_{Si} are the total number of Nb and Si atoms in the surface layer, respectively, which can be further expressed as $N_{\mathrm{Nb}} = n^{BL}_{\mathrm{Nb}} + n^{SL}_{\mathrm{Nb}}$ and $N_{\mathrm{Si}} = n^{BL}_{\mathrm{Si}} + n^{SL}_{\mathrm{Si}}$, where n^{BL}_i and n^{SL}_i (i = Nb, Si) are the number of atoms in the bulk layers (BL) and surface layers (SL), respectively. μ represents the chemical potential and $n_n\mu_{\mathrm{Nb}} + n_s\mu_{\mathrm{Si}} = \mu^{\mathrm{bulk}}_{\mathrm{Nb}_{n_n}\mathrm{Si}_{n_s}}$ for a niobium silicide. Furthermore, to form a niobium silicide, the requirements of $\mu_{\mathrm{Nb}} \le \mu^{\mathrm{bulk}}_{\mathrm{Nb}}$ and $\mu_{\mathrm{Si}} \le \mu^{\mathrm{bulk}}_{\mathrm{Si}}$ must be fulfilled, which leads to $\frac{1}{n_n}\left(\mu^{\mathrm{bulk}}_{\mathrm{Nb}_{n_n}\mathrm{Si}_{n_s}} - n_s\mu^{\mathrm{bulk}}_{\mathrm{Si}}\right) \le \mu_{\mathrm{Nb}} \le \mu^{\mathrm{bulk}}_{\mathrm{Nb}}$.

Figure 4a shows the calculated surface energies for the seven different niobium silicides. The α-Nb_5Si_3 surface energy as a function of Nb chemical potential is in good agreement with the previous first-principles results [8]. Interestingly, we find that the surface energies of β-Nb_5Si_3, NbSi, and Nb_6Si_5 are lower than that of α-Nb_5Si_3. From the surface energies, we further investigate the thickness dependence of the nanofilm phase stabilities. First, we obtain the surface formation energy at a different thickness (h), approximately estimated by the distance between the top and bottom surfaces, by changing n^{BL}_{Nb} and n^{BL}_{Si} through the addition of additional bulk layers. Then, the formation energy for the nanofilms of different thicknesses h is obtained by using this quantity in a modified expression for the bulk formation energy (Equation 3). Here, we assume the surface energy is independent of film thickness in the nanofilms, which is reasonable [28] and consistent with our assessments. **Figures 4b** shows the formation energies for the nanofilms with varying thickness. We find the interpolated formation energies for the bulk compositions agree well with our DFT calculations, which further confirms the reliability of the approximation. In addition, we find that the dependencies do not change irrespective of the surface energy and the Nb chemical potential in Eq (3). At large thickness, we find α-Nb_5Si_3 is stable, consistent with the bulk phase diagram reporting high stability of this phase.

In contrast, the Nb_6Si_5 phase is stable for nanofilms. Therefore, we predict a thickness-dependent phase transition occurs at approximately 1 nm mainly driven by the lower surface energy of Nb_6Si_5.

The stability of the Nb_6Si_5 nanofilm with decreasing thickness has not been previously reported but can be justified because of its significantly lower surface energy compared to α-Nb_5Si_3. In addition, we find that the low surface energy of β-Nb_5Si_3 makes it competitive with α-Nb_5Si_3 and Nb_6Si_5 nanofilms as the film thickness decreases.

One way to synthesize nanoscale niobium silicides is *via* thin film deposition of several monolayers of Nb from a metallic source. The favorable silicide composition that forms depends on deposition method and temperature, assuming a constant niobium flux and unit sticking coefficient, which permits aggregation of adatoms to form a conformal layer, along with Si diffusion. To assess thermal stability, we calculated the formation free energies of nanofilms of α-Nb_5Si_3, β-Nb_5Si_3, Nb_3Si_2, and Nb_6Si_5, using the same method employed to evaluate bulk thermal stability (**Methods** and **Figure S2** [40]). **Figure 5a** shows that the entropic contributions in nanofilm Nb_6Si_5 are greater than those of the other nanoscale silicides. The entropy increment with increasing temperature is largely due to vibrational contributions. We find Nb_6Si_5 has a lower Debye temperature of 435 K versus 460 K for bulk α-Nb_5Si_3 obtained from our phonon calculations [11,43,44] (**Table S18** [40]). **Figure 5b** shows this effect leads to a critical thickness of 1.2 nm where the α-Nb_5Si_3 to-Nb_6Si_5 transition occurs, which decreases to a critical thickness of 1 nm when the vibrational-free-energy contribution is omitted at finite temperature (**Figure 4b**). Although β-Nb_5Si_3 and Nb_3Si_2 are also favored compared to α-Nb_5Si_3 at high temperatures (**Figure 5a**), we do not predict a thickness-dependent transition to occur between these phases. However, we have neglected the effects of the Si-silicide interface that may act to template and further favor the formation of one silicide phase over another.

Analysis of the DOS provides a postulate for why the surface energy of Nb_6Si_5 is lower than that of α-Nb_5Si_3. Since there is no adsorption or reconstruction, the change in surface energy is a result of the redistribution of delocalized electrons near the surface. This redistribution enhances the degree of metal-metal bonding character, influences the Fermi level position, and may partly compensate the energy penalty because the metal-metal interaction is crucial to stabilize an intermetallic compound. [35,45–48]As can be seen from **Figure 6a**, the DOS around the Fermi level at the α-Nb_5Si_3(001) surface of the 2.4 nm nanofilm becomes higher than that of the bulk (see **Figure 2a**), which indicates that the Nb-Nb *d* orbital interactions are weaker at the surface [35,45–48]. From our pCOHP analysis, we find that the Nb-Nb *d* orbital interactions are non-bonding for both the bulk and surface structures in α-Nb_5Si_3. A non-bonding state itself does not stabilize the surface structure, but the high DOS at the Fermi level in the intermetallic compounds may result in a magnetic instability [36,49–52], and the high DOS can be reduced by forming a magnetically ordered state that will help with compensating the energy penalty. Interestingly, **Figures 6b** and **6c** show that the DOS and pCOHP, respectively, present a completely different scenario for the Nb_6Si_5 (100) surface structure of a 1.5 nm film. Although there is also an increase in the number of states around the Fermi level, the Nb-Nb *d* orbital interactions in the surface layers exhibit bonding character, which can directly help stabilize the surface structure and partly compensate for the change in coordination in Nb_6Si_5. This change in chemical bonding at the surface likely explains why the surface energy of Nb_6Si_5 is lower than that of α-Nb_5Si_3.

Magnetism in niobium silicides

As mentioned above, the high DOS at the Fermi level in the intermetallic compounds may result in a magnetic instability. We now investigate possible magnetism at the surfaces of α-Nb_5Si_3 and Nb_6Si_5. To find the possible magnetic structures for the two compositions, we rely on a crystal orbital Hamilton population (COHP) analysis, which is usually adopted for analyzing the magnetic ground states of the intermetallic compounds [36,49–52]. **Figure 7** shows the electronic structures and projected COHPs (pCOHPs) for the surface structures of nanofilms of α-Nb_5Si_3 (~2.4 nm) and Nb_6Si_5 (~1.5 nm). We find the Fermi level located in a region of non-bonding states in the electronic structure of the non-magnetic surface of α-Nb_5Si_3. In contrast, the Fermi level is in the bonding states for the non-magnetic configuration of the Nb_6Si_5 surface. Thus, given a large number of states at the Fermi level and the position relative to the bonding and non-bonding states (**Figures 6a** and **6c**), we expect the nanoscale silicides to be susceptible to different magnetic states. In particular, α-Nb_5Si_3 should favor an antiferromagnetic spin configuration, and Nb_6Si_5 should be non-magnetic (or weakly paramagnetic) according to previous electronic structure studies on the magnetic transition metals and intermetallic binary compounds [36,49–52]. Therefore, we focus on understanding the magnetic state of α-Nb_5Si_3.

The reduced coordination from broken bonds at the surface may enhance the effective electron-electron interactions in the silicides. Therefore, we performed DFT+U calculations, which showed sizable magnetic moments confined to the surface niobium atoms for $U \geq 3$ eV despite the strong metallicity. This high U value is reasonable compared with the 4-eV adopted in previous studies of niobium oxides [53]. The final magnetic configurations were determined by random spin generation and symmetry-constraint spin generation (see **Figure S6** [40]). We find an antiferromagnetic spin order for α-Nb_5Si_3 (**Figure 7c**), which collapses to a non-magnetic solution for $U \leq 2.5$ eV, because the metallicity competes with local moment formation on the surface Nb atoms. To understand the origin of the itinerant antiferromagnetic state at the surface, we further calculate the pCOHPs for two scenarios: (i) no magnetic moments and $U = 3$ eV and (ii) with magnetic moments at $U = 3$ eV. **Figures 7a** and **7b** show that the local Coulomb interaction from the $+U$ reduces the density of states (DOS) at the Fermi level in α-Nb_5Si_3. In α-Nb_5Si_3, we find increased interaction strength U does not induce a Stoner ferromagnetic instability because the non-bonding states at the Fermi level favor an antiferromagnetic spin order. Spin polarization of the electronic structure would not lead to energy stabilization if the frontier orbitals are non-bonding in character. This finding is consistent with previous COHP analysis on the intermetallic compounds, leading to a further decease of the DOS at the Fermi level [36,49–52]. Although the magnetic surface structure of α-Nb_5Si_3 and the role of the on-site repulsion U require future experimental validation, our analysis shows that the formation of a 2D spin-density wave reduces the size of the Fermi surface and further stabilizes the surface structure (**Figure 7d**). Here, we find that the formation energy of α-Nb_5Si_3 can be lowered by 13 meV/atom at 2.4 nm compared to the non-magnetic state. Furthermore, the calculated magnetic moment on the surface niobium atoms is approximately 0.24 μ_B/Nb, which could be further decreased in the experiment at finite temperature because of the effects of the spin fluctuations that are not included in our model [54,55].

While magnetism can be one source of qubit decoherence, metallicity can also contribute to decoherence [3,4]. Therefore, we investigate the thickness-dependent metallicity by examining the DOS at the Fermi level (g_F). The values range from 0.4 – 0.8 states per surface atom per eV, which is comparable to 0.2 – 0.3 states per atom per eV of the prototypical metals Al and Au [56,57], but lower than 2.7 states per atom per eV of 2D $MoSi_2$ nanofilms [28]. As can be seen from **Figure 8**, g_F decreases with decreasing nanofilm thickness for both α-Nb_5Si_3 and Nb_6Si_5, suggesting that the nanofilms are more resistive than their bulk counterparts.

Experimental characterization of niobium silicide nanofilms

To experimentally evaluate our computational findings, we prepared 40 nm Nb thin films on Si (111) substrates using DC sputtering and characterized the Nb/Si interface with transmission electron microscopy (TEM) and X-ray reflectivity (XRR). Annular dark-field scanning TEM images reveal an amorphous interfacial layer between the crystalline Si substrate and the crystalline Nb thin film with an approximate thickness of 1.5 nm, as shown in **Figure 9**. Analysis of the interfacial layer by energy-dispersive X-ray spectroscopy (EDS) indicates an elemental composition of 54 ± 1 at. % Nb and 46 ± 1 at. % Si. This composition is consistent with the Nb_6Si_5 stoichiometry. Analysis of the film by XRR reveals a layer stack consisting of 2.4 nm Nb_2O_5, 1.3 nm NbO, 38.5 nm Nb, and 1.2 nm Nb_xSi_y, on bulk Si, from top to bottom (**Figure 10**). The thickness of the Nb/Si interfacial layer as measured by XRR is in good agreement with the value determined by TEM. The XRR measured electron density of the Nb_xSi_y layer is 1.866 $e^{-}Å^{-3}$, which agrees to within 3% of the predicted value for Nb_6Si_5 (1.816 $e^{-}Å^{-3}$). In comparison, Nb_3Si would have a 7% higher and $NbSi_2$ a 20% lower predicted electron density than measured.

CONCLUSION

By performing first-principles calculations, we predict two stable compositions with decreasing thickness in the nanofilm: α-Nb_5Si_3 at larger thickness and Nb_6Si_5 at lower thickness. The critical thickness for the transition between stable nanofilm compositions is around 1 nm and 1.2 nm at 0 K and 700 K, respectively. The stable Nb_6Si_5 phase is also consistent with experimental XRR and TEM measurements, whose thickness is about 1.2 nm. Therefore, our work suggests that Nb-Si heterointerfaces in 2D transmon structures obtained by sputter depositing Nb films on silicon substrates may not be atomically sharp, which has likely implications for achieving long qubit-coherence times. Furthermore, we also predict that α-Nb_5Si_3 nanofilms may be antiferromagnetic, whereas Nb_6Si_5 nanofilms are nonmagnetic based on bond-character analysis.

ACKNOWLEDGMENTS

This material is based upon work supported by the U.S. Department of Energy, Office of Science, National Quantum Information Science Research Centers, Superconducting Quantum Materials and Systems Center (SQMS) under contract No. DE-AC02-07CH11359. Simulations were performed using the high-performance computers from the National Energy Research Scientific Computing Center (NERSC), a U.S. Department of Energy Office of Science User Facility located at

Lawrence Berkeley National Laboratory, operated under Contract No. DE-AC02-05CH11231. This work made use of the EPIC and Keck facilities of Northwestern University's NU*ANCE* Center and the XRD Facility, which receives support from the Soft and Hybrid Nanotechnology Experimental (SHyNE) Resource (NSF ECCS-1542205); the MRSEC program (NSF DMR-1720139) at the Materials Research Center; the International Institute for Nanotechnology (IIN); the Keck Foundation and the State of Illinois. D.P.G. gratefully acknowledges support from the IIN Postdoctoral Fellowship and International Institute for Nanotechnology at Northwestern University.

REFERENCES

[1] A. A. Murthy, J.-Y. Lee, C. Kopas, M. J. Reagor, A. P. McFadden, D. P. Pappas, M. Checchin, A. Grassellino, and A. Romanenko, *TOF-SIMS Analysis of Decoherence Sources in Nb Superconducting Qubits*, Applied Physics Letters **120**, 044002 (2021).

[2] A. Romanenko, R. Pilipenko, S. Zorzetti, D. Frolov, M. Awida, S. Belomestnykh, S. Posen, and A. Grassellino, *Three-Dimensional Superconducting Resonators at T < 20 MK with Photon Lifetimes up to τ = 2 s*, Physical Review Applied **10**, 34032 (2020).

[3] W. D. Oliver and P. B. Welander, *Materials in Superconducting Quantum Bits*, MRS Bulletin **38**, 816 (2013).

[4] D. R. Heslinga and T. M. Klapwijk, *Schottky Barrier and Contact Resistance at a Niobium/Silicon Interface*, Applied Physics Letters **54**, 1048 (1989).

[5] F. Nava, P. A. Psaras, K. N. Tu, H. Takai, S. Valeri, and O. Bisi, *Electrical and Structural Characterization of Nb-Si Thin Alloy Film*, Journal of Materials Research **1**, 327 (1986).

[6] L. Xu, R. Lingling, G. Sitian, Z. Liqi, and T. Xingfu, Strain Study of Nb-Si {001} Interface Based on Geometric Phase Analysis, 2018.

[7] D. S. Wisbey, J. Gao, M. R. Vissers, F. C. S. da Silva, J. S. Kline, L. Vale, and D. P. Pappas, *Effect of Metal/Substrate Interfaces on Radio-Frequency Loss in Superconducting Coplanar Waveguides*, Journal of Applied Physics **108**, 093918 (2010).

[8] S. Y. Liu, J. X. Shang, F. H. Wang, S. Liu, Y. Zhang, D. Li, D. Shields, W. Xue, Y. Liu, H. Dang, and S. Wang, *Oxidation of the Two-Phase Nb/Nb5Si3 Composite: The Role of Energetics, Thermodynamics, Segregation, and Interfaces*, Journal of Chemical Physics **138**, 014708 (2013).

[9] Y. Chen, T. Hammerschmidt, D. G. Pettifor, J. X. Shang, and Y. Zhang, *Influence of Vibrational Entropy on Structural Stability of Nb-Si and Mo-Si Systems at Elevated Temperatures*, Acta Materialia **57**, 2657 (2009).

[10] S. Prasad and A. Paul, *Growth Mechanism of Phases by Interdiffusion and Diffusion of Species in the Niobium-Silicon System*, Acta Materialia **59**, 1577 (2011).

[11] B. Wan, F. Xiao, Y. Zhang, Y. Zhao, L. Wu, J. Zhang, and H. Gou, *Theoretical Study of Structural Characteristics, Mechanical Properties and Electronic Structure of Metal (TM = V, Nb and Ta) Silicides*, Journal of Alloys and Compounds **681**, 412 (2016).

[12] S. L. Wang and Y. Pan, *Insight into the Structures, Melting Points, and Mechanical Properties of NbSi2 from First-Principles Calculations*, Journal of the American Ceramic Society **102**, 4822 (2019).

[13] T. Nakanishi, M. Takeyama, A. Noya, and K. Sasaki, Formation of Metal-Rich Siilicides in the Initial Stage of Interfacial Reactions in Nb/Si Systems, 1995.

[14] N. Suresh, D. M. Phase, A. Gupta, and S. M. Chaudhari, *Electron Density Fluctuations at Interfaces in Nb/Si Bilayer, Trilayer, and Multilayer Films: An x-Ray Reflectivity Study*, Journal of Applied Physics **87**, 7946 (2000).

[15] R. J. Grylls, B. P. Bewlay, H. A. Lipsitt, and H. L. Fraser, *Characterization of Silicide Precipitates in Nb-Si and Nb-Ti-Si Alloys*, Philosophical Magazine A: Physics of Condensed Matter, Structure, Defects and Mechanical Properties **81**, 1967 (2001).

[16] Y. Chen, J. X. Shang, and Y. Zhang, *Effects of Alloying Element Ti on α-Nb5Si3 and Nb3Al from First Principles*, Journal of Physics Condensed Matter **19**, 016215 (2007).

[17] T. Proslier, J. A. Klug, J. W. Elam, H. Claus, N. G. Becker, and M. J. Pellin, *Atomic Layer Deposition and Superconducting Properties of NbSi Films*, Journal of Physical Chemistry C **115**, 9477 (2011).

[18] M. E. Schlesinger, H. Okamoto, A. International, A. B. Gokhale, and R. Abbaschian, Section If: Phase Diagram Evaluations The Nb-Si (Niobium-Silicon) System, 1993.

[19] *[2105.09890] Transmon Qubit with Relaxation Time Exceeding 0.5 Milliseconds*, https://arxiv.org/abs/2105.09890.

[20] A. P. M. Place, L. V. H. Rodgers, P. Mundada, B. M. Smitham, M. Fitzpatrick, Z. Leng, A. Premkumar, J. Bryon, A. Vrajitoarea, S. Sussman, G. Cheng, T. Madhavan, H. K. Babla, X. H. Le, Y. Gang, B. Jäck, A. Gyenis, N. Yao, R. J. Cava, N. P. de Leon, and A. A. Houck, *New Material Platform for Superconducting Transmon Qubits with Coherence Times Exceeding 0.3 Milliseconds*, Nature Communications **12**, 1779 (2021).

[21] J. Sun, R. C. Remsing, Y. Zhang, Z. Sun, A. Ruzsinszky, H. Peng, Z. Yang, A. Paul, U. Waghmare, X. Wu, M. L. Klein, and J. P. Perdew, *Accurate First-Principles Structures and Energies of Diversely Bonded Systems from an Efficient Density Functional*, Nature Chemistry 2016 8:9 **8**, 831 (2016).

[22] J. Sun, A. Ruzsinszky, and J. P. Perdew, *Strongly Constrained and Appropriately Normed Semilocal Density Functional*, Physical Review Letters **115**, 036402 (2015).

[23] G. Kresse and J. Furthmüller, *Efficient Iterative Schemes for* Ab Initio *Total-Energy Calculations Using a Plane-Wave Basis Set*, Physical Review B **54**, 11169 (1996).

[24] G. Kresse and J. Furthmüller, *Efficiency of Ab-Initio Total Energy Calculations for Metals and Semiconductors Using a Plane-Wave Basis Set*, Computational Materials Science **6**, 15 (1996).

[25] G. Kresse and D. Joubert, *From Ultrasoft Pseudopotentials to the Projector Augmented-Wave Method*, Physical Review B **59**, 1758 (1999).

[26] P. E. Blöchl, *Projector Augmented-Wave Method*, Physical Review B **50**, 17953 (1994).

[27] A. I. Liechtenstein, V. I. Anisimov, and J. Zaanen, *Density-Functional Theory and Strong Interactions: Orbital Ordering in Mott-Hubbard Insulators*, Physical Review B **52**, R5467 (1995).

[28] L.-F. Huang and J. M. Rondinelli, *Stable MoSi 2 Nanofilms with Controllable and High Metallicity*, RAPID COMMUNICATIONS PHYSICAL REVIEW MATERIALS **1**, 63001 (2017).

[29] L.-F. Huang and J. M. Rondinelli, *Electrochemical Phase Diagrams for Ti Oxides from Density Functional Calculations*, Physical Review B **92**, 245126 (2015).

[30] L.-F. Huang, X.-Z. Lu, E. Tennessen, and J. M. Rondinelli, *Editor's Choice An Efficient Ab-Initio Quasiharmonic Approach for the Thermodynamics of Solids*, Computational Materials Science **120**, 84 (2016).

[31] Eva Huang, Munlika Satjapipat, and Shubo Han, and F. Zhou*, *Surface Structure and Coverage of an Oligonucleotide Probe Tethered onto a Gold Substrate and Its Hybridization Efficiency for a Polynucleotide Target*, Langmuir **17**, 1215 (2001).

[32] A. Nelson and IUCr, *Co-Refinement of Multiple-Contrast Neutron/X-Ray Reflectivity Data Using MOTOFIT*, Urn:Issn:0021-8898 **39**, 273 (2006).

[33] A. V. Mudring and J. D. Corbett, *Unusual Electronic and Bonding Properties of the Zintl Phase Ca 5Ge3 and Related Compounds. A Theoretical Analysis*, Journal of the American Chemical Society **126**, 5277 (2004).

[34] U. Häussermann, V. F. Kranak, and K. Puhakainen, *Hydrogenous Zintl Phases: Interstitial Versus Polyanionic Hydrides*, Zintl Phases **139**, 143 (2011).

[35] Y. Chen, J. X. Shang, and Y. Zhang, *Bonding Characteristics and Site Occupancies of Alloying Elements in Different Nb5 Si3 Phases from First Principles*, Physical Review B - Condensed Matter and Materials Physics **76**, 184204 (2007).

[36] S. Steinberg and R. Dronskowski, *The Crystal Orbital Hamilton Population (COHP) Method as a Tool to Visualize and Analyze Chemical Bonding in Intermetallic Compounds*, Crystals.

[37] R. Dronskowski and P. E. Bloechl, *Crystal Orbital Hamilton Populations (COHP): Energy-Resolved Visualization of Chemical Bonding in Solids Based on Density-Functional Calculations*, Journal of Physical Chemistry **97**, 8617 (2002).

[38] V. L. Deringer, A. L. Tchougréeff, and R. Dronskowski, *Crystal Orbital Hamilton Population (COHP) Analysis As Projected from Plane-Wave Basis Sets*, Journal of Physical Chemistry A **115**, 5461 (2011).

[39] P. Ravindran and R. Asokamani, *Correlation between Electronic Structure, Mechanical Properties and Phase Stability in Intermetallic Compounds*, Bulletin of Materials Science **20**, 613 (1997).

[40] See Supplemental Material at http://link.aps.org/supplemental/10.110.3/X.XXX.X for details of the phonon spectra for the select bulk and nanofilm niobium silicides; determination of the surface

directions; determination of the surface terminations; determination of the Debye temperatures of Nb, Si, α-Nb_5Si_3 and Nb_6Si_5; determination of the spin orders in α-Nb_5Si_3.

[41] T. A. Manz and N. G. Limas, *Introducing DDEC6 Atomic Population Analysis: Part 1. Charge Partitioning Theory and Methodology*, RSC Advances **6**, 47771 (2016).

[42] N. G. Limas and T. A. Manz, *Introducing DDEC6 Atomic Population Analysis: Part 2. Computed Results for a Wide Range of Periodic and Nonperiodic Materials*, RSC Advances **6**, 45727 (2016).

[43] C. Toher, J. J. Plata, O. Levy, M. de Jong, M. Asta, M. B. Nardelli, and S. Curtarolo, *High-Throughput Computational Screening of Thermal Conductivity, Debye Temperature, and Grüneisen Parameter Using a Quasiharmonic Debye Model*, Physical Review B **90**, 174107 (2014).

[44] I. Papadimitriou, C. Utton, and P. Tsakiropoulos, *The Impact of Ti and Temperature on the Stability of Nb5Si3 Phases: A First-Principles Study*, Science and Technology of Advanced Materials **18**, 467 (2017).

[45] P. Ravindran and R. Asokamani, Correlation between Electronic Structure, Mechanical Properties and Phase Stability in Intermetallic Compounds, 1997.

[46] V. L. Moruzzi, P. Oelhafen, and A. R. Williams, Stability in Ordered and Amorphous Transition-Metal Compounds, 1983.

[47] T. Hong, T. J. Watson-Yang, X.-Q. Guo, A. J. Freeman, and T. Oguchit, Crystal Structure, Phase Stability, and Electronic Structure of Ti-Al Intermetallics: Ti3A1, 1991.

[48] W. Speieri, L. Kumart $, D. D. Sarmai, R. A. de Grootll, and J. C. Fugglell, The Electronic Structure of 4d and 5d Silicides Related Content The Electronic Structure of 4d and 5d Silicides, 1989.

[49] R. Dronskowski, K. Korczak, H. Lueken, and W. Jung, Chemically Tuning between Ferromagnetism and Antiferromagnetism by Combining Theory and Synthesis in Iron/Manganese Rhodium Borides**, 2002.

[50] M. Amsler, S. S. Naghavi, and C. Wolverton, *Prediction of Superconducting Iron-Bismuth Intermetallic Compounds at High Pressure*, Chemical Science **8**, 2226 (2017).

[51] V. Y. Verchenko, A. A. Tsirlin, D. Kasinathan, S. v. Zhurenko, A. A. Gippius, and A. v. Shevelkov, *Antiferromagnetic Ground State in the MnGa4 Intermetallic Compound*, Physical Review Materials **2**, 044408 (2018).

[52] Z. Ryżyńska, J. R. Chamorro, T. M. McQueen, P. Wiśniewski, D. Kaczorowski, W. Xie, R. J. Cava, T. Klimczuk, and M. J. Winiarski, *RuAl6- An Endohedral Aluminide Superconductor*, Chemistry of Materials **32**, 3805 (2020).

[53] C. P. Koçer, K. J. Griffith, C. P. Grey, and A. J. Morris, *First-Principles Study of Localized and Delocalized Electronic States in Crystallographic Shear Phases of Niobium Oxide*, Physical Review B **99**, 075151 (2019).

[54] W. F. Goh and W. E. Pickett, *Competing Magnetic Instabilities in the Weak Itinerant Antiferromagnetic TiAu*, Physical Review B **95**, 205124 (2017).

[55] W. F. Goh and W. E. Pickett, *A Mechanism for Weak Itinerant Antiferromagnetism: Mirrored van Hove Singularities*, EPL **116**, 27004 (2016).

[56] D. Kienle and A. W. Ghosh, *Atomistic Modeling of Metal-Nanotube Contacts*, Journal of Computational Electronics **4**, 97 (2005).

[57] T. Genieys, M. Sentis, and O. Utéza, *Investigation of Ultrashort Laser Excitation of Aluminum and Tungsten by Reflectivity Measurements*, Applied Physics A: Materials Science and Processing **126**, 263 (2020).

Table 1. Structural information for select niobium silicide phases. Here g_F^{Nb-d} represents the density of states per Nb-*d* orbital at the Fermi level. Units of electron density are eÅ^{-3}. Information for the Nb_2Si, γ-Nb_5Si_3 and Nb_5Si_4 surface structures are not shown because of their high surface energies. "—" indicates not applicable.

Composition	**Space group**	**Metallic**	g_F^{Nb-d}	**Electron density**	**Zintl phase**	**Zintl anion(s)**	**Surface plane**	**Surface termination**
Nb_3Si	$P4_2/n$	Yes	0.69	2.001	No	—	(001)	Nb+Si
Nb_2Si	$I4/mcm$	Yes	0.51	1.951	Yes	Si_2^{4-}	(111)	—
α-Nb_5Si_3	$I4/mcm$	Yes	0.41	1.907	Yes	Si_2^{6-}, Si^{4-}	(001)	Si
β-Nb_5Si_3	$I4/mcm$	Yes	0.41	1.919	Yes	Si_2^{4-}, Si^{4-}	(001)	Nb+Si
γ-Nb_5Si_3	$P6_3/mcm$	Yes	0.70	1.890	Yes	Si_2^{4-}	(001)	—
Nb_3Si_2	$P4/mbm$	Yes	0.95	1.892	Yes	Si_2^{6-}	(001)	Nb+Si
Nb_5Si_4	$P4_12_12$	Yes	0.65	1.827	Yes	Si_2^{6-}	(001)	—
Nb_6Si_5	$Ibam$	Yes	0.67	1.816	Yes	Si_4^{4-}, Si_2^{4-}, ${Si'}_2^{4-}$	(100)	Nb+Si
NbSi	$Pnma$	Yes	0.80	1.785	Yes	Si_2^{4-}	(100)	Nb+Si
$NbSi_2$	$P6_222$	Yes	0.68	1.575	No	—	(001)	Nb+Si

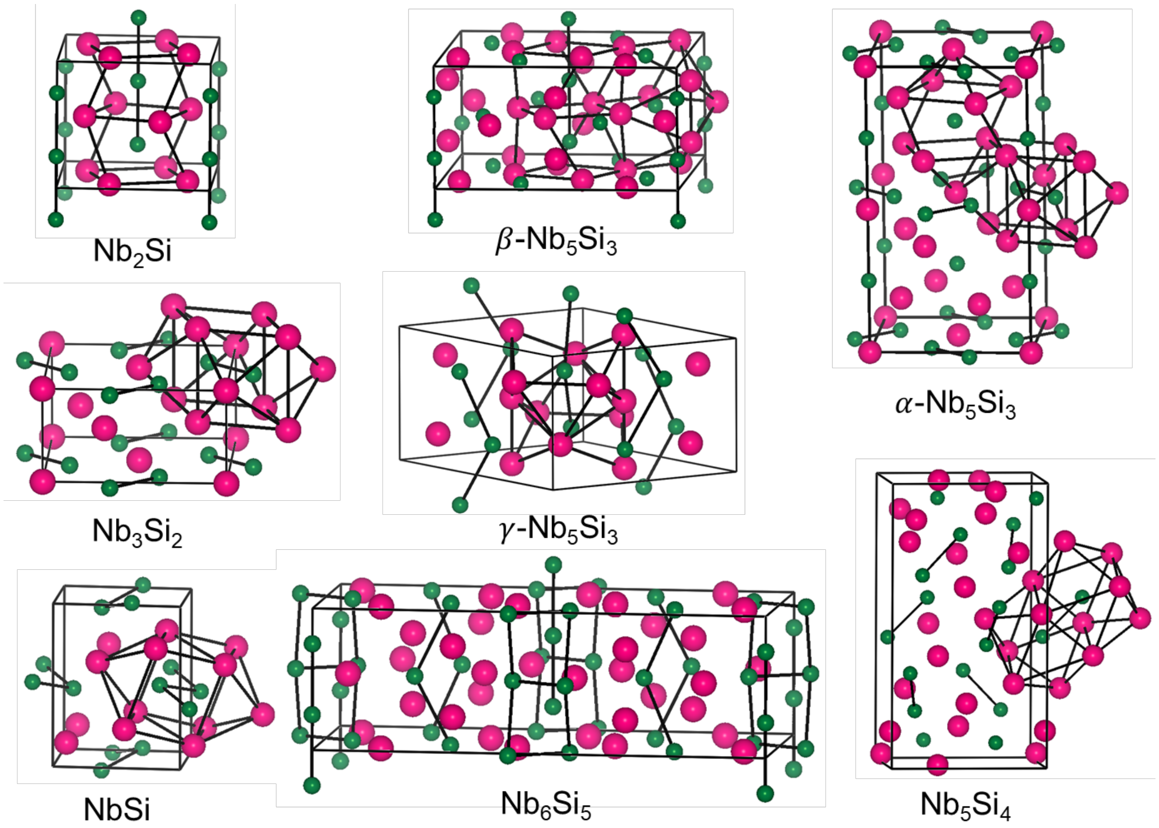

Figure 1. The Zintl phases for 10 select niobium silicides with Nb and Si indicated by pink and green spheres, respectively. The Nb_n polyhedra around the Zintl anions in each phase are indicated except for in the Nb_6Si_5 phase. The Nb polyhedra around polyanionic groups Si_2^{4-} and Si'^{4-}_2 can be found in the other phases, such as the Nb polyhedron in Nb_2Si about Si_2^{4-} and the Nb polyhedron in Nb_5Si_3-γ about Si'^{4-}_2.

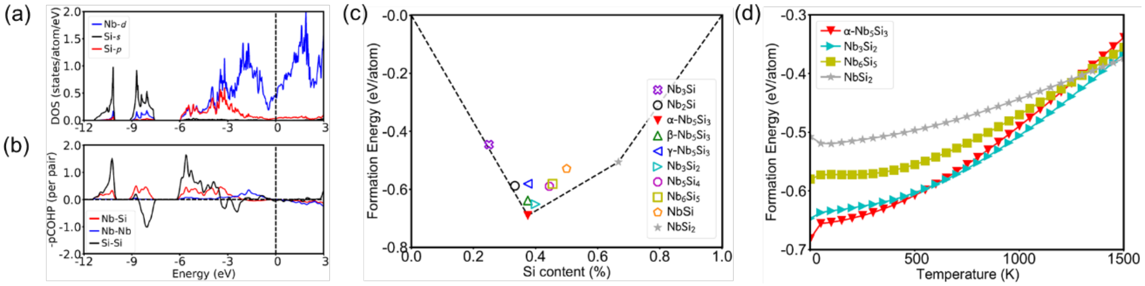

Figure 2. (a) Projected density of states (PDOS) for α-Nb_5Si_3 and its (b) pCOHP with positive, negative, and zero values indicating bonding, antibonding, and non-bonding interactions for the specified atom pair. (c) The DFT-SCAN 0 K Nb-Si convex hull for ten niobium silicide phases is formed by α-Nb_5Si_3 and $NbSi_2$. (d) Formation free energy as a function of temperature with respective to bulk Nb and Si following Equation (6) in **Methods**. The small changes near 0 K in (d) are due to the electronic entropic contributions in Equation (6), which are usually neglected, but included here.

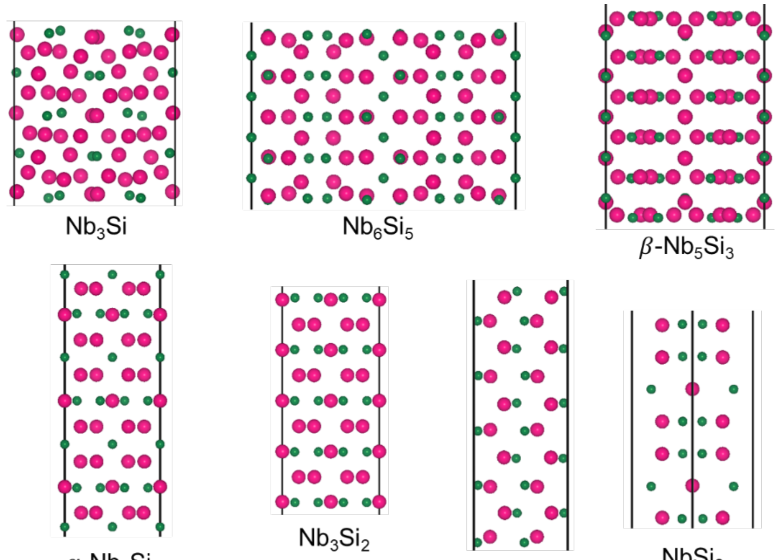

Nb_3Si Nb_6Si_5 β-Nb_5Si_3

α-Nb_5Si_3 Nb_3Si_2 NbSi $NbSi_2$

Figure 3. Slab structures for the specified niobium silicide compositions with nominal thickness of 1.5-2.4 nm.

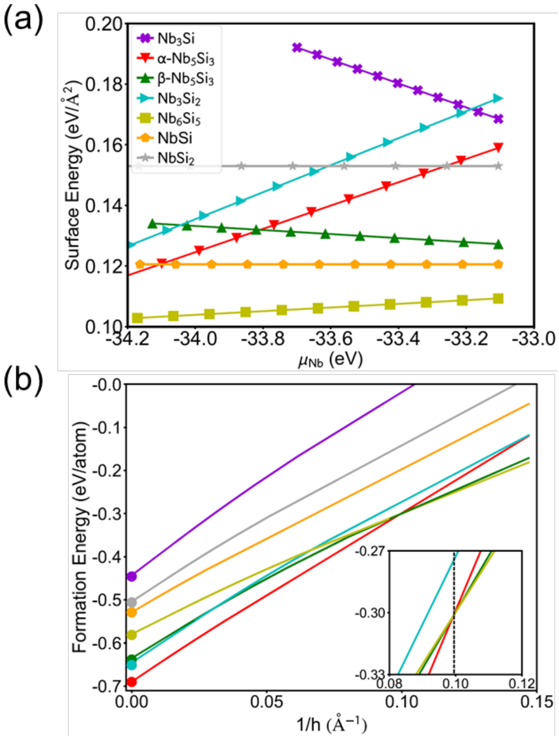

Figure 4. (a) Surface energy as a function of the chemical potential of Nb without finite temperature effects included for the various silicides. (b) The formation energy versus the inverse of the thickness, h^{-1}, which is obtained by performing DFT at 0K. The filled circle at h^{-1}=0 for each composition corresponds to its bulk formation energy. Inset in (b): Enlargement of thickness-dependent crossover happened between -0.33 eV/atom and -0.27 eV/atom in the inversed thickness range from 0.08 Å^{-1} to 0.12 Å^{-1}, where the transition is from α-Nb_5Si_3 to Nb_6Si_5 at approximately 0.1 Å^{-1} as indicated by the dashed vertical line.

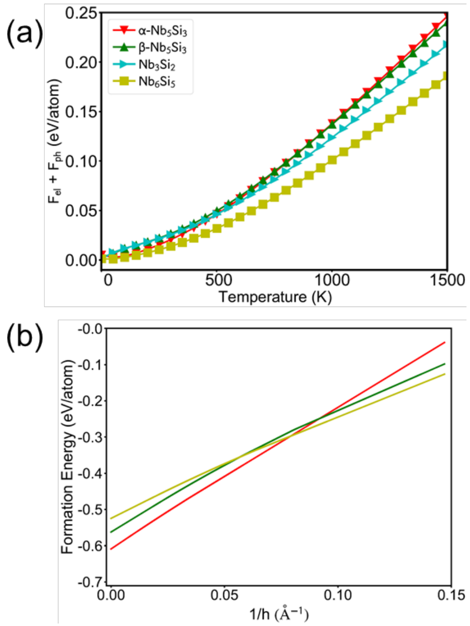

Figure 5 (a) The entropic electronic and phononic contributions to the nanoscale silicide formation energy as a function of the temperature for nanofilms of α-Nb_5Si_3 (2.37 nm), β-Nb_5Si_3 (1.52 nm), Nb_3Si_2 (1.75 nm), and Nb_6Si_5 (1.56 nm). (b) Formation energy versus inverse of the thickness in the Nb rich region including entropic effects at 700 K shows a transition. Here, we predict the formation energy from 0 K to 700 K with a uniform shift for the thickness range considered, where the uniform values are the entropic electronic and phononic contributions at 700 K at 1.56 nm and 2.37 nm for Nb_6Si_5 and α-Nb_5Si_3, respectively. The formation energy at 700 K for β-Nb_5Si_3 is also shown to indicate finite-temperature effects do not stabilize it over Nb_6Si_5 nanofilms.

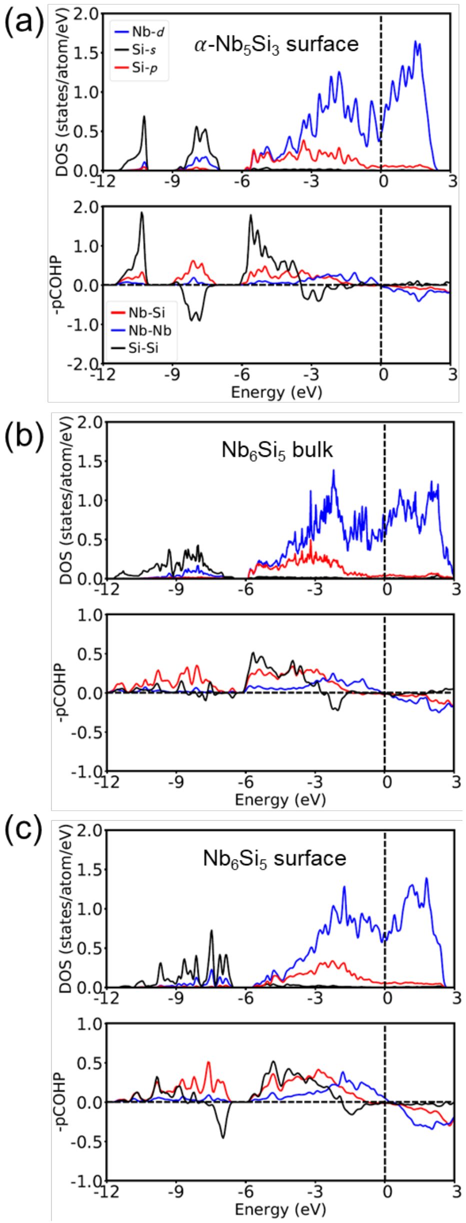

Figure 6. (a) PDOS and pCOHP for the α-Nb_5Si_3(001) surface of the 2.4 nm nanofilm. PDOS and pCOHP for (b) bulk Nb_6Si_5 and (c) Nb_6Si_5 (100) surface of the 1.5 nm nanofilm.

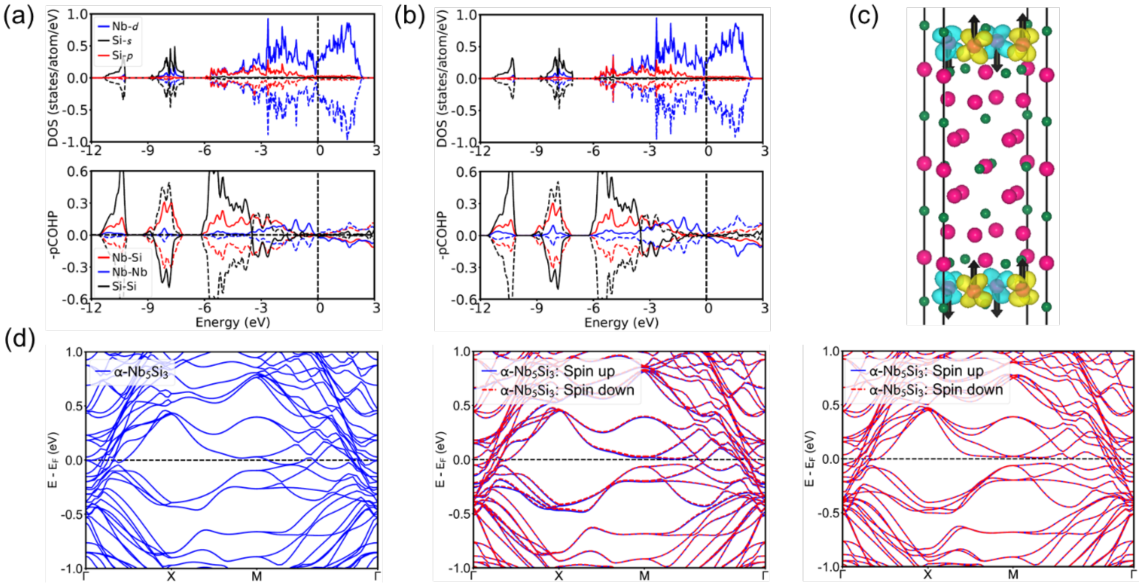

Figure 7. (a) PDOS and pCOHP for the α-Nb$_5$Si$_3$(001) surface with zero magnetic moments at the DFT+*U*=3 eV level. Positive (Negative) DOS indicates the spin-up (spin-down) channel. The positive, zero, and negative values in the pCOHP indicate bonding, non-bonding, and antibonding interactions, respectively, for the spin-up channel in solid lines. The meaning is reversed for the spin-down channel indicated in broken lines. (b) PDOS and pCOHP for the α-Nb$_5$Si$_3$ (001) surface with an antiferromagnetic surface spin structure at the DFT+*U*=3 eV level. (c) shows the spin density distributions of the antiferromagnetic interactions on the α-Nb$_5$Si$_3$ surface. Yellow spin density indicates spin-up and blue indicates spin-down electrons. The resolution for the isosurface plot is 0.0028 eV Å^{-3}. The black arrows indicate the alignment of the spins without considering spin-orbital effects. (d) The band structure for α-Nb$_5$Si$_3$ with (left) non-magnetic, (center) magnetic with no magnetic moments, and (right) antiferromagnetic surface spin configurations.

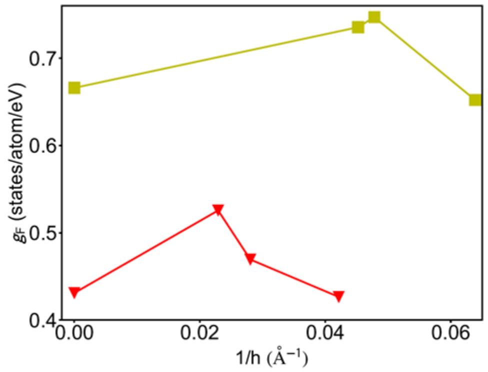

Figure 8. Number of states at the Fermi level as a function of the inverse of the thickness in α-Nb_5Si_3 (red) and Nb_6Si_5 (yellow). Here, the states are counted only from Nb in the structure we computed at each thickness for an accurate prediction of the changes of metallicity, because almost all of the DOS at the Fermi level is from Nb.

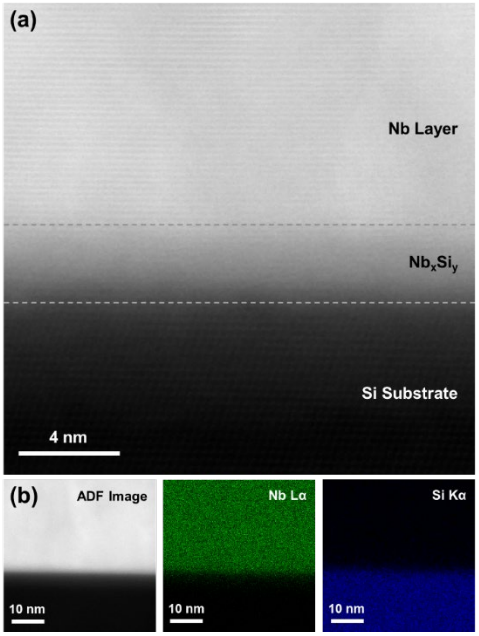

Figure 9. (a) High- and (b) low-magnification annular dark-field STEM images of the amorphous Nb/Si interface (outlined in gray) present in DC sputter deposited Nb thin films on Si(111). Energy-dispersive X-ray spectroscopy (EDS) of Nb (green) and Si (blue) revealed a Nb-rich composition at the interface with 54 ± 1 at. % Nb and 46 ± 1 at. % Si.

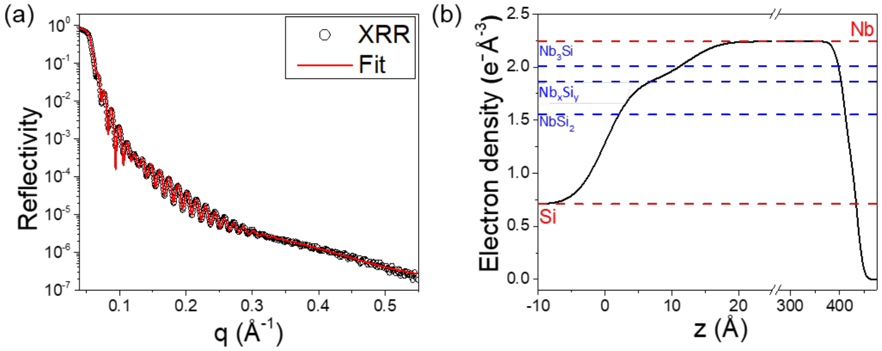

Figure 10. (a) X-ray reflectivity (XRR) of the 40 nm Nb thin film on Si (111). The fitting resulted in 1.2 nm Nb_xSi_y, 38.5 nm Nb, 1.3 nm NbO, and 2.4 nm Nb_2O_5, from bottom to top of the film. (b) Electron density slab profile for the multiple interfaces in the film. The electron density of the Nb_xSi_y layer is 1.866 e^-Å^{-3}.